INSTITUTE OF PHYSICS PUBLISHING JOURNAL OF OPTICS B: QUANTUM AND SEMICLASSICAL OPTICS

J. Opt. B: Quantum Semiclass. Opt. **3** (2001) 251–259 PII: S1464-4266(01)19934-9

Quantum versus classical descriptions of sub-Poissonian light generation in three-wave mixing

Jiří Bajer[1] **and Adam Miranowicz**[2,3]

[1] Department of Optics, Palacký University, 17. listopadu 50, 772 00 Olomouc, Czech Republic
[2] CREST Research Team for Interacting Carrier Electronics, School of Advanced Sciences, The Graduate University for Advanced Studies (SOKEN), Hayama, Kanagawa 240-0193, Japan
[3] Nonlinear Optics Division, Institute of Physics, Adam Mickiewicz University, 61-614 Poznań, Poland

Received 8 December 2000, in final form 13 June 2001
Published 23 July 2001
Online at stacks.iop.org/JOptB/3/251

Abstract
Sub-Poissonian light generation in non-degenerate three-wave mixing is studied numerically and analytically within quantum and classical approaches. Husimi Q-functions and their classical trajectory simulations are analysed to reveal a special regime corresponding to the time-stable sub-Poissonian photocount statistics of the sum-frequency mode. Conditions for the observation of this regime are discussed. Theoretical predictions of the Fano factor and explanation of the extraordinary stabilization of the sub-Poissonian photocount behaviour are obtained analytically by applying the classical trajectories. Scaling laws for the maximum sub-Poissonian behaviour are found. Noise suppression levels in non-degenerate versus degenerate three-wave mixing are discussed on different time scales compared to the revival times. It is shown that the non-degenerate conversion offers much better stabilization of the suppressed noise in comparison to the degenerate process.

Keywords: Sub-Poissonian statistics, three-wave mixing, Fano factor, classical trajectories

1. Introduction

For almost four decades, since the pioneering experiments of Franken *et al* [1] and theoretical foundations laid down by Bloembergen *et al* [2], multiwave mixing has unceasingly been in the forefront of quantum-optical investigations [3,4]. In particular, three-wave mixing (TWM) has attracted considerable interest as a parametric non-linear process of conversion of two sub-frequency (say, ω_1 and ω_2) photons into one sum-frequency ($\omega_1 + \omega_2 \to \omega_3$) photon, together with the inverse process. TWM can be observed in non-linear crystals like ADP, KDP, $LiNbO_3$ or $BaTiO_3$ [5]. Both the total energy, $\hbar\omega_1 + \hbar\omega_2 = \hbar\omega_3$, and momentum, $\hbar\boldsymbol{k}_1 + \hbar\boldsymbol{k}_2 = \hbar\boldsymbol{k}_3$, of interacting photons are conserved. TWM is observable for proper orientations of light beam polarizations and crystal axes [4], therefore it can be considered as a parametric process. TWM is used for the frequency-up conversion if $\omega_1 \to \omega_3$ or the frequency-down conversion if $\omega_3 \to \omega_1$. The process is also useful for the generation of non-classical light such as squeezed, sub-Poissonian and antibunched light [6].

Before the computer era, quantum dynamics was usually investigated under the short-time approximation only. Nowadays, the Taylor series of quantum operators can be found for almost any number of terms with the help of fast computers and sophisticated software. However, these series are usually convergent for short evolution times or even for initial time only. Thus, numerical quantum methods (see, e.g., [7]) fail in the simulation of long-time quantum evolution. On the other hand, as we have shown in [8,9], the method of classical trajectories gives very good estimation in the case of strong-field interaction (practically, for photon numbers larger than 10). The computational speed of the classical-trajectory method does not depend on the numbers of interacting photons and, moreover, for a larger number of photons obtains better precision. Thus, the method is very fast and offers a simple substitute for the tedious exact quantum numerical calculations. The classical-trajectory method enables not only numerical but also some analytical predictions, e.g., for stationary Fano factors [8, 9] or for maximum pump depletion in TWM [10]. A method similar to ours to simulate classical noise in TWM was used by Chmela [11].

In previous papers, we have studied degenerate processes of wave mixing, including the second [8] and higher [9] harmonic generations. Here, we generalize the former results for non-degenerate wave mixing. It is well-known that both degenerate and non-degenerate TWM can be used for the generation of sub-Poissonian light [12, 13]. Nevertheless, theoretical predictions of quantum parameters, like the Fano factor, are most often derived under the short-interaction (short-time or short-length) approximation (see, e.g., [12–14]), thus valid for weak non-linear coupling of the optical fields only. Motivated by papers of Nikitin and Masalov [15] and of Bandilla, Drobný and Jex [16, 17], we analyse the long-interaction evolution of TWM. The main result of this article can be summarized as follows: the TWM can be a source of time-stable sub-Poissonian light of the sum-frequency mode in the no-energy-transfer regime. The deepest noise reduction, with the Fano factor equal to 5/6, can be observed for the balanced input amplitudes $r_1 = r_2 = r_3/\sqrt{2}$. The same degree of photocount noise suppression in the sum-frequency mode can be achieved for degenerate TWM. However, the sub-Poissonian light produced in non-degenerate TWM is better stabilized compared to that in degenerate TWM. Moreover, the Fano factors for the sub-frequency modes in non-degenerate TWM are smaller than those for the degenerate process. This and other results will be demonstrated analytically by applying a method of classical trajectories and tested numerically within the quantum approach.

2. Quantum analysis

In the quantum approach, non-degenerate three-wave mixing can be described by the interaction Hamiltonian (e.g., [12])

$$\hat{H} = \hbar g \left(\hat{a}_1 \hat{a}_2 \hat{a}_3^\dagger + \hat{a}_1^\dagger \hat{a}_2^\dagger \hat{a}_3 \right), \qquad (1)$$

where $\hat{a}_k$ and $\hat{a}_k^\dagger$ denote, respectively, annihilation and creation operators of the sub-frequency (labelled with subscript 1, 2) and sum-frequency (subscript 3) modes; g is a non-linear coupling parameter, which is related to the quadratic susceptibility tensor $\chi^{(2)}$ of a given non-linear optical crystal and also dependent on the geometry of the laboratory set-up [4].

As in [9], we analyse the quantum Fano factors given by $F_k = (\langle \hat{n}_k^2 \rangle - \langle \hat{n}_k \rangle^2)/\langle \hat{n}_k \rangle$ for a photon-number operator $\hat{n}_k = \hat{a}_k^\dagger \hat{a}_k$. The light is referred to as sub-Poissonian if $F_k < 1$ and super-Poissonian if $F_k > 1$.

For weak non-linear interactions or short crystal, the short-time approximation can be applied for analytical predictions of photocount noise suppression with $F_k < 1$ [12, 13]. The Fano factors are approximated by

$$F_{1,2} = 1 + 2r_3^2 (gt)^2 + \tfrac{8}{3} r_1 r_2 r_3 \sin\theta \, (gt)^3 + \mathcal{O}\{(gt)^4\},$$
$$F_3 = 1 - \tfrac{4}{3} r_1 r_2 r_3 \sin\theta \, (gt)^3 + \mathcal{O}\{(gt)^4\}, \qquad (2)$$

where r_k are the input coherent amplitudes and $\theta = \phi_1 + \phi_2 - \phi_3$ is the input phase mismatch. For $\sin\theta > 0$, the sub-Poissonian statistics in the sum-frequency mode can be observed. For $\theta = 0$, we find the higher-order short-time Fano factor expansion to be

$$F_3 = 1 + \left(r_3^2 - 7r_1^2 r_2^2 + 4r_1^2 r_3^2 + 4r_2^2 r_3^2 \right) \frac{(gt)^4}{3} + \mathcal{O}\{(gt)^5\}.$$

It is seen that the sub-Poissonian light in the sum-frequency mode is generated for some combinations of input amplitudes r_k. Since the Fano factors depend weakly on time (i.e., in its third or higher-order power), it is difficult to observe the sub-Poissonian light generation in the short-time regime.

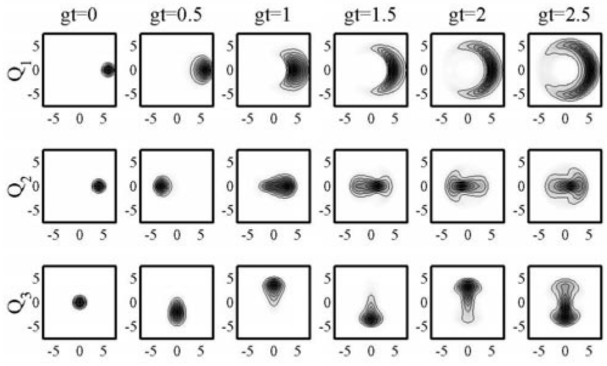

Figure 1. Quantum dynamics *out* of NETR: cross sections of single-mode Q-functions: $Q_1(\mathrm{Re}\alpha_1, \mathrm{Im}\alpha_1)$ and $Q_2(\mathrm{Re}\alpha_2, \mathrm{Im}\alpha_2)$ for sub-frequency mode and $Q_3(\mathrm{Re}\alpha_3, \mathrm{Im}\alpha_3)$ for sum-frequency mode at different scaled evolution times for initial coherent fields with real amplitudes, $\alpha_k(0) = r_k$, set to $r_1 = 6$, $r_2 = 4$ and $r_3 = 0$.

To analyse the exact quantum dynamics of the TWM process beyond the short-time approximation, we apply the Walls–Barakat method [3] of Hamiltonian diagonalization for the initial coherent states. Quantum analysis enables numerical estimation of all statistical properties including photocount noise. Complete quantum information of TWM dynamics can be given by the Husimi Q-function defined to be

$$Q(\alpha_1, \alpha_2, \alpha_3) = \pi^{-3} \langle \alpha_1, \alpha_2, \alpha_3 | \hat{\rho} | \alpha_1, \alpha_2, \alpha_3 \rangle, \qquad (3)$$

where $|\alpha_1\rangle \otimes |\alpha_2\rangle \otimes |\alpha_3\rangle$. In figures 1 and 2, we plot its marginal single-mode Husimi Q-functions given by

$$Q(\alpha_k) = \int Q(\alpha_1, \alpha_2, \alpha_3) \prod_{m \neq k} \mathrm{d}^2\alpha_m, \qquad (4)$$

where $k, m = 1, 2, 3$. The Fano factors, presented in figures 3 and 4, were calculated with the help of the marginal Q-functions. Due to obvious computational difficulties, the exact quantum results can be obtained for relatively small numbers (up to a few hundred) of interacting photons only.

By analysing the numerical quantum solution we observe that the basic features of the photon number evolution for

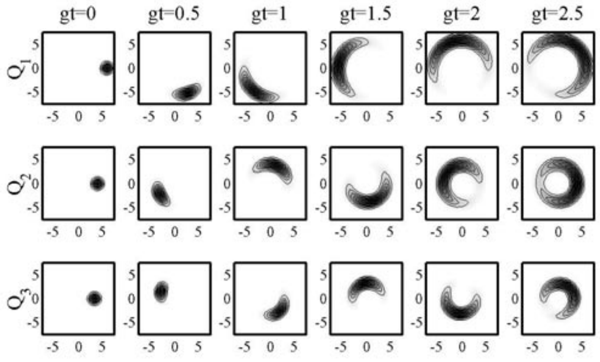

Figure 2. Quantum dynamics *in* NETR: cross sections of marginal Q-functions as in figure 1, but for $r_1 = 6$, $r_2 = 4$, and $r_3 = r_1 r_2/\sqrt{r_1^2 + r_2^2} \approx 3.328$.

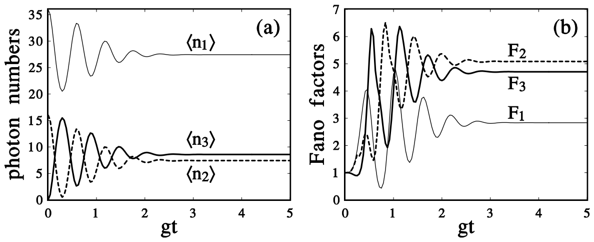

Figure 3. Quantum dynamics *out* of NETR: (a) photon numbers $\langle \hat{n}_k \rangle$ and (b) Fano factors F_k $(k = 1, 2, 3)$ for coherent inputs with real amplitudes $r_1 = 6$, $r_2 = 4$, and $r_3 = 0$. For longer times, all the modes become stationary with the super-Poissonian statistics, $F_k > 1$.

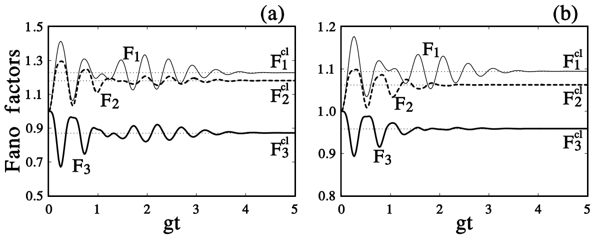

Figure 4. Quantum dynamics *in* NETR: Fano factors F_1 (thin-solid curve), F_2 (dashed curve), and F_3 (thick-solid curve) versus scaled time for different amplitudes of initial coherent fields: (a) $r_1 = 6$, $r_2 = 4$, and (b) $r_1 = 6$, $r_2 = 2$ together with $r_3 = r_1 r_2/\sqrt{r_1^2 + r_2^2}$. The sub-frequency mode becomes super-Poissonian, $F_{1,2} > 1$. By contrast, the sum-frequency mode becomes sub-Poissonian, $F_3 < 1$. Dotted lines represent the classical trajectory predictions of $F_k^{\rm cl}$ to which all the quantum curves tend asymptotically.

non-degenerate TWM are in agreement with those for the harmonic generation processes, as recently reported in [8,9]. In particular, we observe the so-called no-energy-transfer regime (NETR) [16–18], for which the energies and intensities of both modes remain constant in time during the interaction. Although small energy flows between the modes appear as a consequence of vacuum fluctuations, their influence is negligible for strong fields. NETR in three-wave mixing can be observed if the amplitudes and phases of the initial coherent fields are matched as follows (equation (18) in [16]):

$$\frac{1}{r_3^2} = \frac{1}{r_1^2} + \frac{1}{r_2^2},$$
$$\phi_3 = \phi_1 + \phi_2. \tag{5}$$

Usually, i.e., for the initial coherent fields *not* satisfying (5), all the Fano factors are stabilized in the super-Poissonian statistics after a short ($gt\,|r_k| \lesssim 1$) relaxation period. Thus, the outputs have high-level photocount noise. In figure 1, we present a typical quantum evolution of the single-mode Husimi functions $Q(\alpha_1)$ and $Q(\alpha_1)$ for the initial amplitudes $r_1 = 6$, $r_2 = 4$ and $r_3 = 0$. The corresponding evolutions of the photon numbers and Fano factors are presented in figure 3.

Different behaviour is observed if the initial phase ϕ_3 and amplitude r_3 of the sum-frequency mode fulfil the condition for NETR. This distinction is clearly seen by comparing figures 1 and 2 for Q-functions or figures 3 and 4 for the Fano factors. In figure 4, the Fano factors are calculated for two different pairs of the initial amplitudes of sub-frequency modes: (a) $r_1 = 6$, $r_2 = 4$ and (b) $r_1 = 6$, $r_2 = 2$ and the sum-frequency-mode amplitude r_3 fulfilling (5). We observe that all the Fano factor curves start at $F_k\,(0) = 1$ and after some relaxations become stationary at much lower noise levels than those for fields out of NETR. The sub-frequency mode remains super-Poissonian with $F_{1,2}\,(t) > 1$, whereas the sum-frequency mode becomes sub-Poissonian with $F_3\,(t) < 1$. The most suppressed noise is observed for the balanced inputs, given by $r_1 = r_2$ and $r_3 = r_1/\sqrt{2}$, as a special case of condition (5). For those inputs, the Fano factor in the time limit tends to $F_3\,(t \to \infty) \approx 0.83$.

As we have shown in [8, 9], the same degree of the Fano factor can be obtained in degenerate TWM. Thus, one can address the following objection: Why study the same parameter in the closely related non-degenerate version? First, we stress that the same Fano factor is obtained in a special case only: for the sum-frequency mode in NETR for long-interaction times and high-intensity fields. By contrast, these factors are distinct for the sub-frequency mode under the same initial conditions. In general, the results even for the sum-frequency mode in these two processes are different for initial conditions either not fulfilling (5) or for lower intensity fields or different time periods. Second, we will show that the Fano factors for non-degenerate TWM are better stabilized than those for degenerate TWM for much longer evolution times. This is an important advantage of the non-degenerate conversion.

For better comparison, let us analyse in detail degenerate TWM described by

$$\hat{H}' = \hbar g' \left(\hat{a}_1^2 \hat{a}_3^\dagger + \hat{a}_1^{\dagger 2} \hat{a}_3 \right). \tag{6}$$

For clarity, observables calculated for degenerate TWM are marked with prime to distinguish them from those for model (1) and we keep subscript 3 (not 2) for the sum-frequency mode. Hamiltonian (6) formally differs from (1) in the assumption of $\hat{a}_1 = \hat{a}_2$ only. But we also put $g' = g/\sqrt{2}$ for better synchronization of oscillations in photon numbers $\langle \hat{n}_k' \rangle$ and $\langle \hat{n}_k \rangle$. Sub-Poissonian statistics in degenerate TWM were analysed in our former works [8, 9]. In figures 5 and 6, we compare exact quantum evolutions of the mean photon

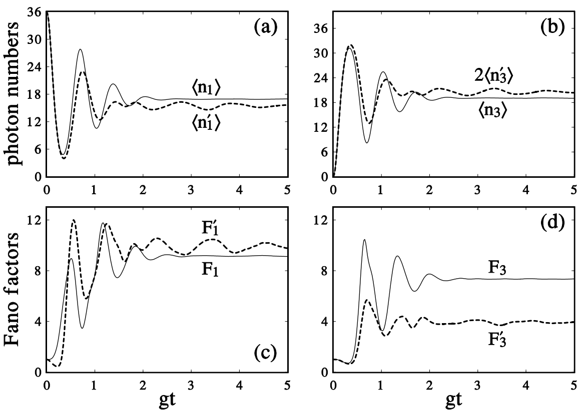

Figure 5. Non-degenerate versus degenerate TWM *out* of NETR: Photon numbers $\langle\hat{n}_k\rangle$ and Fano factors F_k ($k = 1, 3$) are obtained for initial amplitudes $r_1 = r_2 = 6$ and $r_3 = 0$, whereas $\langle\hat{n}'_k\rangle$ and F'_k are for $r'_1 = 6$ and $r'_3 = 0$. All quantities with (without) prime correspond to degenerate (non-degenerate) TWM.

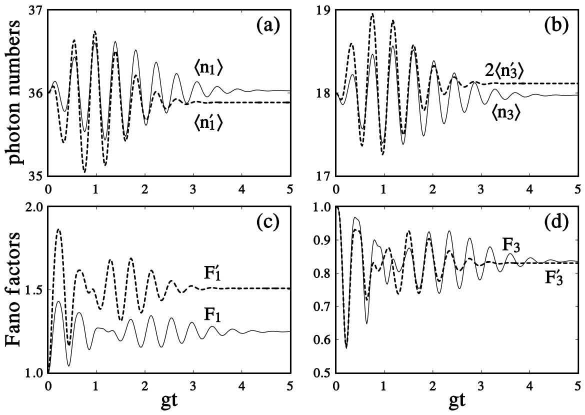

Figure 6. Non-degenerate versus degenerate TWM *in* NETR: $\langle\hat{n}_k\rangle$ and F_k are calculated for initial amplitudes $r_1 = r_2 = 6$ and $r_3 = 6/\sqrt{2}$, whereas $\langle\hat{n}'_k\rangle$ and F'_k are for $r'_1 = 6$ and $r'_3 = 3$.

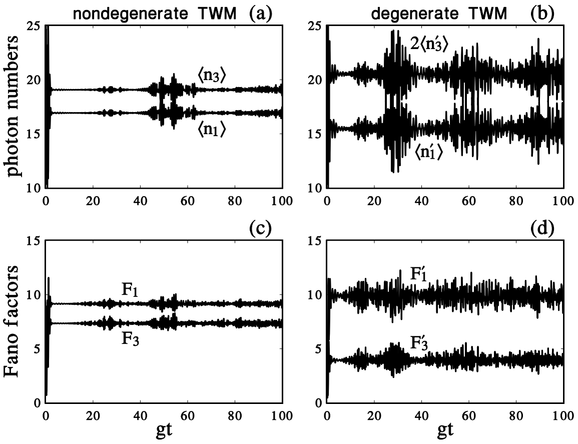

Figure 7. Revivals and collapses in degenerate TWM versus those in non-degenerate TWM *out* of NETR. Initial conditions are the same as in figure 5.

numbers and Fano factors for degenerate ($\langle\hat{n}'_k\rangle$ and F'_k for $k = 1, 3$) and non-degenerate ($\langle\hat{n}_k\rangle$ and F_k) TWM for the same initial conditions. We observe similar behaviour for short times $gt \ll 1$ only. For longer times (also for $gt < 1$) results are not equal by any means. Different predictions of quantum evolutions for models (1) and (6) come from different commutation relations: $[\hat{a}_1, \hat{a}_2^\dagger] = 0$ for non-degenerate TWM and $[\hat{a}_1, \hat{a}_2^\dagger] \equiv [\hat{a}_1, \hat{a}_1^\dagger] = 1$ for degenerate TWM. As a result, constants of motion are different: $\hat{N}'_{\text{total}}(t) \equiv \hat{n}'_1(t) + 2\hat{n}'_3(t) = \text{const}$ for degenerate TWM, whereas $\hat{n}_1(t) - \hat{n}_2(t) = \text{const}$ and $\hat{n}_1(t) + \hat{n}_3(t) = \text{const}$ for non-degenerate TWM. We note that $\hat{N}_{\text{total}}(t) \equiv \hat{n}_1(t) + \hat{n}_2(t) + \hat{n}_3(t) \neq \text{const}$ in the latter process. Evolutions, presented in figures 5 and 6 for degenerate and non-degenerate TWM, are distinct in amplitudes and frequency of oscillations as well as in the level of their ‘saturation’. For example, the limiting value of the sum-frequency Fano factor for degenerate TWM is lower than that for non-degenerate TWM for evolution out of NETR (see figure 5(d)). While the sub-frequency Fano factor in NETR is considerably higher for degenerate compared to non-degenerate TWM (see figure 6(c)).

In figures 1–6, we have analysed the time regime which is long compared to the typical interaction times for known crystal lengths. However, the time is short compared to the revival times for such systems. The question arises about the photon-number noise suppression on such a long scale. This analysis will show an advantage of non-degenerate over degenerate TWM related to the stabilization of the suppressed photon-number noise. In figures 7 and 8, we present the long-time evolution for $0 < gt < 100$ of the mean photon numbers and Fano factors for both non-degenerate ($\langle\hat{n}_k\rangle$ and F_k) and degenerate ($\langle\hat{n}'_k\rangle$ and F'_k) TWM. We observe that the revivals are strongly pronounced for (i) degenerate TWM (right-hand side of figures 7 and 8) compared to the non-degenerate process (left-hand side), and (ii) outside NETR (figure 7) rather than in NETR (figure 8). Thus, the non-degenerate TWM in NETR exhibits the highest stability. Even for longer evolution times as $100 < gt < 1000$ of non-degenerate TWM, the oscillations are similar to those for $0 < gt < 100$ and it is hardly difficult to classify them as a typical revival. Oscillations in $\langle\hat{n}_k\rangle$ are of order 10^{-3} and in F_k are of order 10^{-2} even for such small initial amplitudes equal to $\alpha_1 = \alpha_2 = 6$ and $\alpha_3 = 6/\sqrt{2}$. Our analysis is restricted to initial coherent inputs. It is worth noting that the revivals are much stronger for quantum input fields such as, e.g., Fock states. In conclusion, although the degenerate and non-degenerate TWM lead to approximately the same photon-number noise suppression in the sum-frequency mode for NETR (see figure 6(d)), the non-degenerate process offers much better stabilization of the suppressed noise for long evolution times (compare figures 8(c) and 8(d)).

In the following sections, we will apply an approximate method of classical trajectories to explain the extraordinary stabilization of the observed photocount noise and to estimate analytically the level of noise suppression for NETR.

3. Classical analysis

A complete quantum solution of the model given by Hamiltonian (1) can be found numerically only. Yet, in a

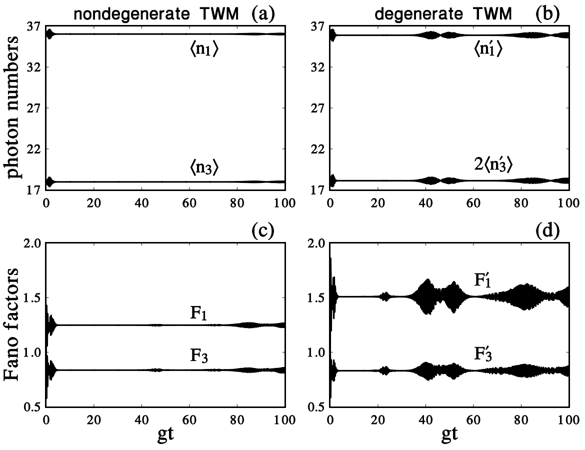

Figure 8. Revivals and collapses in degenerate and non-degenerate TWM *in* NETR with the same initial conditions as those in figure 6.

special case for strong fields, analytical results can be obtained by applying approximate classical methods.

In analogy to quantum Hamiltonian (1), the classical model of non-degenerate TWM can be described by [4]:

$$\mathcal{H} = g\left(\alpha_1\alpha_2\alpha_3^* + \text{c.c.}\right), \tag{7}$$

where α_k are the complex amplitudes of the kth mode and g is a non-linear coupling parameter. From (7), one readily obtains the following complex differential equations

$$\begin{aligned}\dot{\alpha}_1 &= -\mathrm{i}g\alpha_2^*\alpha_3,\\ \dot{\alpha}_2 &= -\mathrm{i}g\alpha_1^*\alpha_3,\\ \dot{\alpha}_3 &= -\mathrm{i}g\alpha_1\alpha_2.\end{aligned} \tag{8}$$

It is easy to show by comparing (8) with equations (12) and (13) from [8] that the classical models for degenerate and non-degenerate TWM are equivalent for $\alpha_1 = \alpha_2$ and arbitrary evolution times. To get equations of motion for degenerate TWM, it is enough to replace g by $\sqrt{2}g'$ and α_3 by $\sqrt{2}\alpha_3'$ in (8). As was discussed in the previous section, the quantum evolutions of degenerate and non-degenerate TWM are equivalent for $gt \ll 1$ only.

By introducing real amplitudes and phases, $\alpha_k = r_k\mathrm{e}^{\mathrm{i}\phi_k}$, equation (8) can be transformed into the following four real equations

$$\begin{aligned}\dot{r}_1 &= -gr_2r_3\sin\theta,\\ \dot{r}_2 &= -gr_1r_3\sin\theta,\\ \dot{r}_3 &= gr_1r_2\sin\theta,\\ \dot{\theta} &= g\left(\frac{r_1r_2}{r_3} - \frac{r_1r_3}{r_2} - \frac{r_2r_3}{r_1}\right)\cos\theta,\end{aligned} \tag{9}$$

where $\theta = \phi_1 + \phi_2 - \phi_3$ is the phase mismatch. The system (9) has three integrals of motion

$$\begin{aligned}E_1 &= r_1^2 + r_3^2 = n_1 + n_3,\\ E_2 &= r_2^2 + r_3^2 = n_2 + n_3,\\ K &= r_1r_2r_3\cos\theta.\end{aligned} \tag{10}$$

By extracting r_1, r_2 and θ from (9), the equation for the remaining amplitude r_3 reads as

$$(r_3\dot{r}_3/g)^2 + K^2 = r_3^2\left(E_1 - r_3^2\right)\left(E_2 - r_3^2\right) \tag{11}$$

or, equivalently, for the intensity $n_3 = r_3^2$ as

$$\begin{aligned}(\dot{n}_3/2g)^2 &= n_3\left(E_1 - n_3\right)\left(E_2 - n_3\right) - K^2\\ &= \left(a - n_3\right)\left(b - n_3\right)\left(n_3 - c\right),\end{aligned} \tag{12}$$

where the numbers $a \geqslant b \geqslant c$ are the roots of the cubic equation $n_3\left(E_1 - n_3\right)\left(E_2 - n_3\right) - K^2 = 0$ satisfying the conditions $abc = K^2$, $a+b+c = E_1 + E_2$, and $ab+ac+bc = E_1E_2$. Then, the solution for $n_3\left(t\right)$ is found to be

$$n_3\left(t\right) = c + \left(b - c\right)\mathrm{sn}^2\left[\sqrt{a-c}\,gt + \phi_0, k\right], \tag{13}$$

where $\mathrm{sn}(u, k)$ is the Jacobi elliptic function with $k = \sqrt{\frac{b-c}{a-c}}$ and ϕ_0 is the initial phase given by the elliptic integral of the first kind

$$\phi_0 = F\left(z, k\right) = \int_0^z \frac{\mathrm{d}x}{\sqrt{1 - k^2\sin^2 x}}, \tag{14}$$

where $z = \arcsin\sqrt{(n_3(0) - c)/(b - c)}$. One observes that n_3 is a periodic function oscillating between the values c and b with the period given by $T = 4F\left(\frac{\pi}{2}, k\right)/g$.

In two special cases, solution (13) reduces to the elementary solutions:

$$n_3\left(t\right) = r^2\tanh^2(rgt) \tag{15}$$

for $r_1 = r_2 = r$ and $r_3 = 0$, and

$$n_3\left(t\right) = r^2\mathrm{sech}^2(rgt) \tag{16}$$

for $r_1 = r_2 = 0$ and $r_3 = r$. Another elementary solution is obtained for the initial fields fulfilling conditions (5). In this case, the solution reads as ($k = 1, 2, 3$)

$$\alpha_k\left(t\right) = r_k\exp\left(-\mathrm{i}\frac{r_1r_2r_3}{r_k^2}\,gt\right), \tag{17}$$

which describes the classical no-energy-transfer regime [18], since the amplitudes and energies of all interacting modes remain constant, i.e., $n_k(t) = |\alpha_k(t)|^2 = r_k^2$. We conclude that the NETR observed in the quantum numerical analysis presented in the previous section corresponds to the classical solution (17).

4. Classical trajectory analysis

Classical solutions, as presented in the previous section, do not describe quantum noise. Nevertheless, they can be used for the simulation of quantum noise if the initial complex amplitudes are chosen randomly. This approach, referred to as the method of classical trajectories, has been applied successfully in a description of noise in various quantum-optical phenomena [8–11, 15–20]. By analysing Q-functions and Fano factors, we will show that the method of classical trajectories properly simulates photocount noise in TWM processes.

To calculate statistical moments, like the Fano factors, one needs to analyse the classical evolution of each process (trajectory) separately and then average the moments over all the obtained trajectories. The classical Fano factor, defined to be

$$F^{\mathrm{cl}} = \frac{\overline{n^2} - \bar{n}^2}{\bar{n}}, \tag{18}$$

can be obtained by classical trajectory averaging. We denote this averaging by bar to distinguish it from quantum ensemble averaging indicated by brackets. We will apply the method of classical trajectories along the lines of the analysis presented in [8]. We choose the initial amplitudes to be $\alpha_k = r_k$ and blur them with the Gaussian noise, which results in

$$\alpha_k = r_k + x_k + \mathrm{i}y_k, \tag{19}$$

where x_k and y_k are mutually independent real Gaussian stochastic quantities with the identical variances $\sigma^2 = 1/4$. We assume further that the fields are strong, i.e., $r_k \gg 1$.

By substituting (19) into (10), the integrals of motion can be expressed as

$$\begin{aligned} E_1 &= |\alpha_1|^2 + |\alpha_3|^2 = r_1^2 + r_3^2 + c_1, \\ E_2 &= |\alpha_2|^2 + |\alpha_3|^2 = r_2^2 + r_3^2 + c_2, \\ K &= \mathrm{Re}\left(\alpha_1 \alpha_2 \alpha_3^*\right) = r_1 r_2 r_3 + d_1, \end{aligned} \tag{20}$$

where c_1, c_2 and d_1 are small corrections of E_1, E_2 and K, respectively, depending on r_k, x_k and y_k. To eliminate the linear term in the right-hand side of (12), we substitute

$$\begin{aligned} n_3 &= \frac{1}{3}E_2 + \frac{1}{3}E_1 - \frac{1}{3}\sqrt{\left(E_2^2 - E_1E_2 + E_1^2\right)} + \epsilon \\ &= n_{30} + b + \epsilon, \end{aligned} \tag{21}$$

where ϵ is a small correction of stationary value $n_{30} + b$. Under the strong-field approximation ($r_k \gg 1$), one can neglect the small correction ϵ^3 and the right-hand side of (12) can be approximated by the quadratic function $\Omega^2\left(a^2 - \epsilon^2\right)$. Thus, one gets the simple equation

$$\dot{\epsilon}^2 = (2g\Omega)^2\left(a^2 - \epsilon^2\right), \tag{22}$$

which leads to the solution of (12) in the following form

$$n_3\left(t\right) = n_{30} + b + a\sin\left(2g\Omega t + \varphi\right), \tag{23}$$

where $n_{30} = r_3^2 = r_1^2 r_2^2/(r_1^2 + r_2^2)$. The coefficients a, b and Ω, together with c_1 and c_2, are complex functions of r_k and noise parameters x_k and y_k. With the help of integrals of motions, given by (10), solutions for other modes ($k = 1, 2$) can readily be found as

$$n_k(t) = E_k - n_3(t) = r_k^2 + c_k - b - a\sin(2g\Omega t + \varphi). \tag{24}$$

We observe that all three solutions, given by (23) and (24), are of the form of large constants slightly perturbed by the same harmonic function. In figures 9 and 10, we present a classical simulation of quantum dynamics by calculating time evolutions of 10 000 points in phase space according to classical equations of motion. These representations correspond to the Husimi Q-functions presented in figures 1 and 2, respectively. By comparing figures 1 and 2 or, equivalently, figures 9 and 10, we observe two distinct types of evolution determined by the initial amplitudes to be in NETR or out of it.

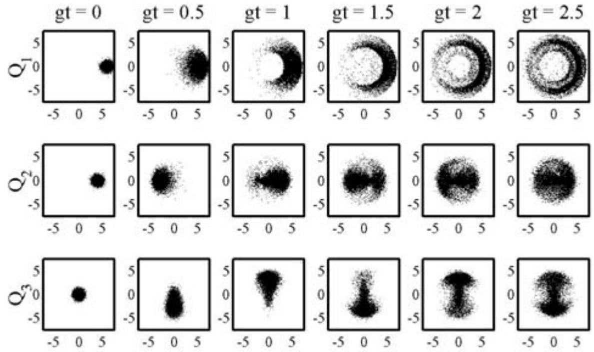

Figure 9. Classical simulation of typical quantum dynamics *out* of NETR: clouds of 10 000 points representing marginal Q-functions for the same initial conditions and times as in figure 1.

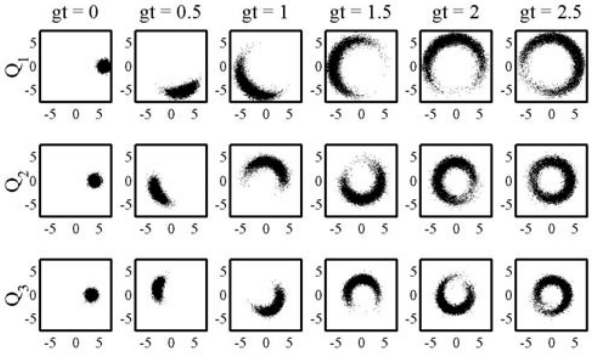

Figure 10. Classical simulation of quantum dynamics *in* NETR for the same cases as in figure 2.

The classical and quantum descriptions are principally different in detail. Thus, our plots of the Q-function based on the exact quantum solution of TWM (figures 1 and 2) and those obtained by an approximate classical simulation (figures 9 and 10) also differ in detail. The discrepancies are more pronounced for lower amplitude inputs and longer interactions. Moreover, the methods of graphical representations are different: a topographical picture of $Q_k(\alpha)$ versus a cloud of classical points. Nevertheless, “it is surprising how close the clouds of dots are to the Q-function” [15]. The clear correspondence between figures 2 and 10 or 1 and 9 justifies our application of the classical trajectory approximation.

As the next step of the classical trajectory method, one has to perform averaging of solutions (23) and (24) to calculate the desired moments. We find that the mean values of the parameters occurring in solution (24) are $\bar{b} = \overline{c_1} = \overline{c_2} = 0$ and

$$\bar{\Omega} = \sqrt{r_1^2 + r_2^2 - r_3^2} = \sqrt{\frac{r_2^4 + r_1^2 r_2^2 + r_1^4}{r_1^2 + r_2^2}} \tag{25}$$

together with their mean quadratic moments

$$\begin{aligned}\overline{b^2} &= \frac{2A}{r_2^2 + r_1^2}(2r_1^8 + r_1^6 r_2^2 + 2r_1^4 r_2^4 + r_1^2 r_2^6 + 2r_2^8),\\ \overline{(c_1-b)^2} &= \frac{2A}{r_2^2}(4r_1^8 + 10r_1^6 r_2^2 + 11r_1^4 r_2^4 + 7r_1^2 r_2^6 + 2r_2^8),\\ \overline{(c_2-b)^2} &= \frac{2A}{r_2^2}(2r_1^8 + 7r_1^6 r_2^2 + 11r_1^4 r_2^4 + 10r_1^2 r_2^6 + 4r_2^8),\\ \overline{a^2} &= 2A(4r_1^6 + 7r_1^4 r_2^2 + 7r_1^2 r_2^4 + 4r_2^6), \qquad (26)\end{aligned}$$

given in terms of the auxiliary function

$$A = \frac{r_1^2 r_2^2}{8(r_1^4 + r_1^2 r_2^2 + r_2^4)^2}\,. \qquad (27)$$

The phase φ can be obtained from (23) at $t = 0$. Thus, the photon-number mean values are simply equal to $\bar{n}_k = r_k^2$ and their variances are given by ($k = 1, 2, 3$)

$$\overline{n_k^2} - \bar{n}_k^2 = \overline{(c_k - b)^2} + \frac{1}{2}\overline{a^2} \qquad (28)$$

in terms of the moments (26) and $c_3 \equiv 0$. The term $\overline{\sin^2(2g\Omega t + \varphi)}$ has simply been estimated as $\frac{1}{2}$ for sufficiently large t, when $\bar{n}_k$ and F_k become time independent. Thus, we arrive at the following Fano factors

$$\begin{aligned}F_1^{\rm cl} &= 1 + A(8r_1^4 + 5r_1^2 r_2^2 + 5r_2^4),\\ F_2^{\rm cl} &= 1 + A(5r_1^4 + 5r_1^2 r_2^2 + 8r_2^4),\\ F_3^{\rm cl} &= 1 - 3A(r_1^2 + r_2^2)^2, \qquad (29)\end{aligned}$$

where A is given by (27). As one could expect, the formulas for $F_k^{\rm cl}$ are symmetric with respect to exchange of the subscripts $1 \longleftrightarrow 2$. We finally conclude that TWM in the no-energy-transfer regime can be a source of time-stable sub-Poissonian light in the sum-frequency mode as described by the Fano factor

$$F_3^{\rm cl}(\rho) = 1 - \frac{3\rho(1+\rho)^2}{8(1+\rho+\rho^2)^2} \leqslant 1, \qquad (30)$$

depending on the ratio of the mean intensities of initial coherent fields defined by $\rho = r_1^2/r_2^2$ if $r_1 > 0$ or $\rho = r_2^2/r_1^2$ if $r_2 > 0$. The sub-frequency fields become super-Poissonian with the Fano factors

$$F_1^{\rm cl}(\rho) = F_2^{\rm cl}(1/\rho) = 1 + \frac{\rho(5 + 5\rho + 8\rho^2)}{8(1+\rho+\rho^2)^2} \geqslant 1. \qquad (31)$$

In figure 11, the classical predictions of the Fano factors are depicted as a function r_1/r_2. By analysing (30) and figures 4, 6, and 11, we conclude that the sum-frequency mode is solely sub-Poissonian ($F_3^{\rm cl} \leqslant 1$) and the strongest noise suppression is obtained for $r_1 = r_2 = r_3/\sqrt{2}$, when $F_3^{\rm cl} = 5/6 \approx 0.833$. For highly unbalanced input intensities $r_1 \ll r_2$ or $r_1 \gg r_2$, all the Fano factors approach unity $F_1^{\rm cl} \approx F_2^{\rm cl} \approx F_3^{\rm cl} \to 1$. Mutually equal Fano factors, estimated by $F_1^{\rm cl} = F_2^{\rm cl} = 5/4 = 1.25$, are predicted for the balanced inputs $r_1 = r_2 = r_3/\sqrt{2}$. The maximum values of the Fano factors, estimated by $F_1^{\rm cl} = F_2^{\rm cl} = \max = 1.255$, are obtained for slightly unbalanced inputs: $r_1 = 1.136r_2$ to maximize $F_1^{\rm cl}$ and for $r_1 = 0.881r_2$ to maximize $F_2^{\rm cl}$.

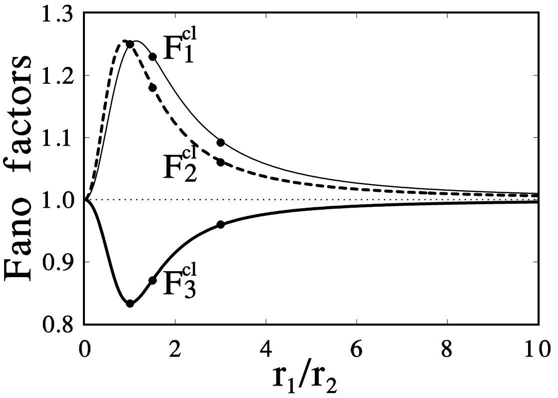

Figure 11. Classical predictions of Fano factors $F_k^{\rm cl}$ ($k = 1, 2, 3$) versus ratio r_1/r_2 of the input coherent-field amplitudes. Small circles represent the quantum Fano factors F_k obtained from the exact quantum solutions presented in figures 4 and 6.

We have predicted in [8, 9] the stationary sub-Poissonian Fano factors for the second ($F_2^{\rm cl} = 5/6$) and third ($F_3^{\rm cl} = 13/16$) harmonic generations within NETR. The minimum value of the sum-frequency-mode Fano factor for non-degenerate TWM is the same as that obtained for degenerate TWM (i.e., second-harmonic generation) [8], but higher than that for degenerate four-wave mixing (i.e., third-harmonic generation). However, for the sub-frequency mode, the Fano factors for non-degenerate TWM are smaller than those for degenerate cases, namely $F_{1,2}^{\rm cl}(1) = 5/4$ instead of 3/2 and 29/16, respectively.

In figures 3 and 4, we have compared evolutions of the exact quantum Fano factors F_k (depicted by solid or dashed curves) with their classical estimations, $F_k^{\rm cl}$ (dotted lines). One observes that all the curves start at $F_k = 1$ for initial coherent fields and after some relaxations become quasi-stationary with $F_k \approx F_k^{\rm cl}$, given by (29). It is worth noting that very good estimation is achieved even for relatively small amplitudes, e.g., $r_k \leqslant 6$. We conclude that the conditions for NETR in quantum dynamics and suppression of the observed quantum noise levels are well explained by the classical trajectory method.

Finally, we will compare scaling properties of the Fano factors in their dependence on light intensity and initial amplitude for degenerate and non-degenerate TWM. Drobný *et al* [17] calculated the scaling laws under the truncated Wigner approximation for the maximum sub-Poissonian photon-number noise in TWM. Their formulas are valid also in the limit of $r = \alpha_1(0) \to \infty$. Here, we focus on nonlinear fits for finite ranges of r only. Let us investigate the scaling properties of the maximum sub-Poissonian character of the sum-frequency mode corresponding to the first minimum of the F_3 and F_3' curves in figures 3(b), 4, 5(d), and 6(d). In figure 12, we plot the exact quantum numerical values of $\min_t F_3(x,t) \equiv F_3(x, t_{\rm min})$ or $\min_t F_3'(x,t) \equiv F_3'(x, t_{\rm min}')$ as a function of initial amplitudes $x = r_1 = r_2 = r_1'$ and of intensities $x \equiv \langle \hat{n}_3(t_{\rm min})\rangle = \langle \hat{n}_3'(t_{\rm min}')\rangle$. We fit those minima with the exponent and polynomial functions of parameters

Table 1. Scaling laws ax^b for non-degenerate TWM ($\min_t F_3(x)$) and degenerate TWM ($\min_t F_3'(x)$) *out* of NETR. Initial conditions are $1 < r_1 = r_2 \leqslant 10$, $1 < r_1' \leqslant 20$, and $r_3 = r_3' = 0$.

No	Fitted function	a	b	Error
1	$\min_t F_3(r_1)$	0.8819	−0.1254	0.0004
2	$\min_t F_3(\langle\hat{n}_3\rangle)$	0.8560	−0.0572	0.0001
3	$\min_t F_3'(r_1')$	0.7694	−0.0906	0.0003
4	$\min_t F_3'(\langle\hat{n}_3'\rangle)$	0.7352	−0.0427	0.0003

Table 2. Polynomial fit $(ax^2 + bx + c)/x^2$ for non-degenerate ($\min_t F_3(x)$) and degenerate ($\min_t F_3'(x)$) TWM *in* NETR. Initial conditions are $1 < r_1 = r_2 \leqslant 10$, $1 < r_1' \leqslant 20$, $r_3 = r_1/\sqrt{2}$, and $r_3' = r_1'/2$.

No	Fitted function	r_1	a	b	c	Error
1	$\min_t F_3(r_1)$	> 1	0.5474	0.1104	0.2956	0.0003
		$\gg 1$	0.5519	0.0643	0.3894	0.0007
2	$\min_t F_3(\langle\hat{n}_3\rangle)$	> 1	0.5562	0.3143	−0.1618	0.0001
		$\gg 1$	0.5559	0.3240	−0.2057	0.0008
3	$\min_t F_3'(r_1')$	> 1	0.5495	0.1195	0.3510	0.0003
		$\gg 1$	0.5541	0.0406	0.5739	0.0012
4	$\min_t F_3'(\langle\hat{n}_3'\rangle)$	> 1	0.5558	0.2057	−0.0607	0.0001
		$\gg 1$	0.5556	0.2121	−0.0783	0.0005

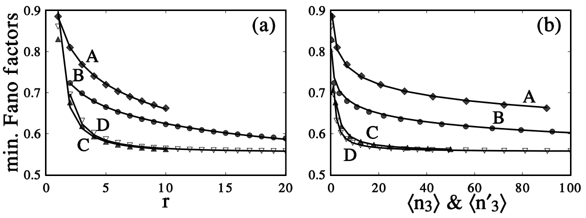

Figure 12. Maximum photon-number noise suppression for non-degenerate (curves A and C) and degenerate (B and D) TWM: Time-minimized Fano factors, $\min_t F_3$ and $\min_t F_3'$, as a function of (a) initial amplitudes $r \equiv r_1 = r_1'$ and (b) mean photon numbers $\langle\hat{n}_3\rangle = \langle\hat{n}_3'\rangle$. Curves: A (with diamonds), initial amplitude $r_3 = 0$; B (with circles), $r_3' = 0$; C (with solid triangles), $r_3 = r_1/\sqrt{2} = r/\sqrt{2}$; D (with empty triangles), $r_3' = r_1'/2 = r/2$. The marked points are obtained from the exact quantum solutions and are fitted with the functions given in tables 1 and 2.

listed in tables 1 and 2. The errors, given in the last column, are estimated by the standard deviation. We observe that the scaling laws ax^b for non-degenerate and degenerate TWM give good approximation of the exact values *out* of NETR only. However, the ax^b law fails to describe with good precision $\min_t F_3(x)$ and $\min_t F_3'(x)$ *in* NETR at least for intensities up to 100 photons. Thus, instead of the exponent law we apply the (inverse) polynomial fit of the form $(ax^2 + bx + c)/x^2$, where we introduce x^{-2} in relation to the definition of the Fano factor. By contrast to the exponent fits, the polynomial laws give very good predictions of the maximum sub-Poissonian behaviour at least for $1 < r_1 = r_2 \leqslant 10$ and $1 < r_1' \leqslant 20$ as seen in figure 12 and table 2. The scaling laws of Drobný *et al* [17] differ slightly from ours presented in table 1. The minor differences in the fitted parameters result from different ranges of r used in the fitting procedures and from application of the truncated Wigner approximation in [17] compared to our exact quantum method.

On the other hand, the Fano factors for the balanced ($r_1 = r_2$) non-degenerate TWM under NETR conditions for long times and high intensity fields do not depend on light intensity, which follows from equations (30) and (31). Similarly, there are no scaling properties of the Fano factors in degenerate TWM for long times and high intensity fields in NETR, i.e., under the same conditions as those assumed in our classical trajectory analysis.

5. Conclusions

We have analysed the long-time interactions in non-degenerate three-wave mixing. To the best of our knowledge, our quantum analysis is the first presentation of the exact and completely quantum solution of non-degenerate three-wave mixing. In literature, a special solution can be found for initial sub-frequency fields with zero amplitudes $\alpha_1 = \alpha_2 = 0$ only. The no-energy-transfer regime for proper choices of amplitudes and phases of the initial coherent fields has been observed. We have compared the evolutions of the Husimi Q-functions and their classical trajectory simulations for processes in the no-energy-transfer regime and out of it. We have shown numerically using the quantum-mechanical approach that three-wave mixing in the no-energy-transfer regime exhibits the time-stable photocount statistics. This phenomenon was explained analytically by applying the method of classical trajectories. We have shown that the sub-frequency mode become super-Poissonian with the Fano factor $F_{1,2} > 1$, whereas the sum-frequency mode becomes sub-Poissonian with $F_3 < 1$. We have found that the most suppressed photocount noise, given by $F_3 \approx 5/6$, is obtained for the balanced initial intensities $r_1^2 = r_2^2$ of the sub-frequency mode and the sum-frequency intensity equal to $r_3^2 = r_1^2/2$ as determined from condition (5) for the no-energy-transfer regime. Scaling laws and polynomial fits for the maximum sub-Poissonian behaviour have been found for different processes and initial conditions. We have compared in detail the non-degenerate and degenerate conversions on time scales short and long compared to the revival times. We have observed that non-degenerate three-wave mixing, contrary to the degenerate conversion, exhibits stabilization of the suppressed photon-number noise even on the revival time scale.

Acknowledgments

We thank Professor Jan Peřina and Dr Ondřej Haderka for helpful discussions. AM is deeply indebted to Professor Nobuyuki Imoto for his hospitality and stimulating research at SOKEN. JB was supported by the Czech Ministry of Education (Grant No LN00A015 and CEZ J14/98) and the Grant Agency of Czech Republic (202/00/0142).

References

[1] Franken P A, Hill A E, Peters C W and Weinreich G 1961 *Phys. Rev. Lett.* **7** 118
Bass M, Franken P A, Ward J F and Weinreich G 1962 *Phys. Rev. Lett.* **9** 446
[2] Armstrong J A, Bloembergen N, Ducuing J and Pershan P S 1962 *Phys. Rev.* **127** 1918
Bloembergen N and Pershan P S 1962 *Phys Rev* **128** 606
Bloembergen N 1965 *Nonlinear Optics* (New York: Benjamin)
[3] Walls D and Barakat R 1970 *Phys. Rev.* A **1** 446
[4] Boyd R W 1991 *Nonlinear Optics* (New York: Academic Press) ch 2
Shen Y R 1984 *The Principles of Nonlinear Optics* (New York: Wiley) ch 8 and 9
Bandilla A, Drobný G and Jex I 1998 *Opt. Commun.* **156** 112
[5] Dmitriev V G, Gurzadyan G G and Nikogosyan D N 1999 *Handbook of Nonlinear Optical Crystals* (Berlin: Springer)
[6] Mandel L and Wolf E 1995 *Optical Coherence and Quantum Optics* (Cambridge: Cambridge University Press) sects 12.10 and 14.9
Peřina J, Hradil Z and Jurčo B 1994 *Quantum Optics and Fundamentals of Physics* (Dordrecht: Kluwer) sect 85
Bachor H A 1998 *A Guide to Experiments in Quantum Optics* (Weinheim: Wiley-VCH Verlag) ch 9
[7] Bajer J and Lisoněk P 1991 *J. Mod. Opt.* **38** 719
[8] Bajer J, Haderka O and Peřina J 1999 *J. Opt. B: Quantum Semiclass. Opt.* **1** 529
[9] Bajer J and Miranowicz A 2000 *J. Opt. B: Quantum Semiclass. Opt.* **2** L10
[10] Bandilla A, Drobný G and Jex I 2000 *J. Opt. B: Quantum Semiclass. Opt.* **2** 265
[11] Chmela P 1996 *Czech J. Phys.* **46** 541
[12] Peřina J 1991 *Quantum Statistics of Linear and Nonlinear Optical Phenomena* (Dordrecht: Kluwer) ch 10
[13] Dewael P 1975 *J. Phys. A: Math. Gen* **8** 1614
Kozierowski M and Tanaś R 1977 *Opt. Commun.* **21** 229
Kielich S, Kozierowski M and Tanaś R 1978 *Coherence and Quantum Optics* vol 4 ed L Mandel and E Wolf (New York: Plenum) p 511
[14] Bajer J and Peřina J 1992 *Opt. Commun.* **92** 99
[15] Nikitin S P and Masalov A V 1991 *Quantum. Opt.* **3** 105
[16] Bandilla A, Drobný G and Jex I 1996 *Opt Comm* **128** 353
[17] Drobný G, Bandilla A and Jex I 1997 *Phys. Rev.* A **55** 78
[18] Paul H 1973 *Nichtlineare Optik II* (Berlin: Academie-Verlag) p 16
[19] Milburn G J 1986 *Phys. Rev.* A **33** 674
Milburn G J and Holmes C A 1986 *Phys. Rev. Lett.* **56** 2237
[20] Sand van de G and Rost J M 2000 *Phys. Rev.* A **62** 053403